Increasing the time resolution of single-molecule experiments with Bayesian inference

Colin D. Kinz-Thompson and Ruben L. Gonzalez, Jr.

Department of Chemistry, Columbia University, New York, NY 10027

To whom correspondence should be addressed: cdk2119@columbia.edu (C.D.K.) and rlg2118@columbia.edu (R.L.G.)

Keywords
Single-Molecule, Bayesian Inference, Temporal Resolution, Missed Events, Ribosome, Transition-State Theory, Markov Chain Monte Carlo, Hidden Markov Model

Abstract

Many time-resolved, single-molecule biophysics experiments seek to characterize the kinetics of biomolecular systems exhibiting dynamics that challenge the time resolution of the given technique. Here we present a general, computational approach to this problem that employs Bayesian inference to learn the underlying dynamics of such systems, even when they are much faster than the time resolution of the experimental technique being used. By accurately and precisely inferring rate constants, our Bayesian Inference for the Analysis of Sub-temporal-resolution Data (BIASD) approach effectively enables the experimenter to super-resolve the poorly resolved dynamics that are present in their data.

Introduction

Given their inherent ability to eliminate ensemble averaging, time-resolved single-molecule biophysical methods have revolutionized the study of biological mechanisms by enabling distributions of molecular properties to be observed, stochastic fluctuations from equilibrium to be investigated, and transiently sampled reaction intermediates to be characterized (1). Generally, the majority of these methods involve making sequential measurements of an experimental signal that acts as a proxy for the underlying, time-dependent state of a biomolecule. As a result, this process yields a time-ordered series of discrete measurements from which the underlying dynamics of the corresponding biomolecule can be inferred (2). Unfortunately, the ability to resolve the continuously varying dynamics of the corresponding biomolecule from a series of discrete measurements is fundamentally limited. Indeed, whereas a biomolecule may exchange between multiple conformational states during a single measurement acquisition period, these states are collectively represented by a single, time-averaged measurement of the experimental signal. This effect is akin to chemical exchange effects in nuclear magnetic resonance (NMR) experiments, in which distinct resonance peaks can coalesce into a single, averaged resonance peak when a nucleus rapidly exchanges between distinct magnetic environments (3). As a result of this effect, many time-resolved, single-molecule biophysical methods often fail to detect or properly characterize mechanistically critical biomolecular processes that occur on or faster than the time resolution of the technique, including early steps in ligand binding, local folding events, and rapid conformational fluctuations (4, 5).

To push beyond the time-resolution limits of these single-molecule methods, we have developed a Bayesian inference-based computational approach, which we call Bayesian Inference for the Analysis of Sub-temporal resolution Dynamics (BIASD), to infer the rate constants governing transitions between discrete states of a single molecule from the analysis of a time-resolved, single-molecule experimental signal–even if those rate constants are substantially faster than the time resolution of the recorded experimental signal. Much

like learning the point spread function describing the fluorescence signal from a single fluorophore in a super-resolution imaging experiment enables the spatial position of the fluorophore to be inferred beyond the spatial resolution of the experiment, learning the model describing the kinetic behavior of a single molecule in a time-resolved single-molecule experiment using BIASD enables the kinetic behavior of the single molecule to be inferred beyond the temporal resolution of the experiment. By using Bayesian inference, BIASD can also integrate information from other experiments to further enhance its resolving power, while also employing a natural framework with which to describe the precision that the amount of data collected during the single-molecule experiment will lend to the determination of the parameters governing the single-molecule kinetics (2, 6, 7). It is worth noting that, in a close parallel to the approach we describe here, Bayesian inference has been previously employed to improve the time resolution of the time-dependent free induction decay in NMR spectroscopy experiments, resulting in an orders-of-magnitude improvement in spectral resolution (7, 8).

Here, we first describe the Bayesian inference-based framework underlying BIASD. We then use BIASD to analyze computer-simulated signal *versus* time trajectories (signal trajectories) and investigate the accuracy and precision with which we can infer the known rate constants for transitions between states that were used to generate the signal trajectories. We next use BIASD to analyze experimentally recorded fluorescence resonance energy transfer efficiency (E_{FRET}) *versus* time trajectories (E_{FRET} trajectories) in order to infer the unknown rate constants for transitions between states in the E_{FRET} trajectories. Notably, the E_{FRET} trajectories that we have analyzed here had previously eluded analysis due to the presence of transitions that are much faster than the time resolution of the electron-multiplying charge-coupled device camera that was used to record them (9). Finally, we describe and demonstrate an extension of the BIASD framework that can be used to infer rate constants for experimental systems consisting of static or interconverting sub-populations of molecular properties within an individual or ensemble of molecules. Remarkably, we find that BIASD permits accurate inference of rates constants from time-resolved, single-molecule experiments, even when the rate constants are orders of magnitude larger than the time resolution of the signal trajectories.

Bayesian Inference-based Framework Underlying BIASD

In biomolecular systems, functional motions—such as those involved in ligand binding and dissociation processes, or large-scale conformational rearrangements—very often involve the simultaneous formation and/or disruption of numerous, non-covalent interactions. The relatively low probability of simultaneously forming and/or disrupting these numerous interactions can therefore result in large, entropically dominated, transition-state energy barriers for such functional motions (10, 11). Consequently, individual biomolecules are generally expected to exhibit effectively discrete and instantaneous transitions between relatively long-lived states (5), an expectation that is consistent with the step-like transitions that are generally observed in time-resolved single-molecule experiments (12).

An important consideration when analyzing the signal trajectories from such single-molecule experiments is that whenever an individual molecule undergoes a transition from one state to another, the transition occurs stochastically during the time period, τ, over which the detector collects and integrates the signal to record a data point in the signal trajectory. Thus, the probability that a transition will coincide exactly with the beginning or end of the τ in which it takes place is essentially zero. As a result, when a transition takes place, the signal value that is recorded during that τ does not solely represent either of the states involved in that transition. Instead, it represents the average of the signal values corresponding to the states that are sampled during τ, weighted by the time spent in each of those states. This time averaging makes it imprudent

to assign the signal value recorded during such a τ to any one particular state, a process called idealization, because the molecule will have occupied multiple states during that τ. Notably, when the rate constants for transitions between states become comparable to or greater than τ^{-1}, there is a large probability that the τs of a signal trajectory will contain one or more transitions, and that, consequently, many of the signal values of the signal trajectory will exhibit this time averaging. Given such a scenario, analysis methods in which individual τs are assigned to particular states (*e.g.*, the widely used strategy of idealizing signal trajectories using signal thresholds (13), or hidden Markov models (HMMs) (14, 15)) will introduce significant errors into the calculated rate constants for transitions between states and into the signal values assigned to those states (2).

In order to overcome the potential errors associated with determining rate constants and signal values from the analysis of signal trajectories, BIASD instead analyzes a different parameter that depends upon the dynamics of the biomolecular system: the fraction of time that is spent in each state during the τs in a signal trajectory (16–21). To illustrate this approach, consider the case of an individual molecule that undergoes stochastic, uncorrelated (*i.e.*, Markovian), and reversible transitions between two states, denoted 1 and 2, (*i.e.*, $1 \rightleftarrows 2$, with forward and reverse rate constants of k_1 and k_2, respectively) that have unique signal values of ϵ_1 and ϵ_2. If the fraction of time that the molecule spends in state 1 during a particular τ is f, then, because of the two-state nature of the system, the fraction of time that the molecule spends in state 2 during that τ is $1-f$. It is important to note that, although the molecule is in an equilibrium between states 1 and 2, the value of f for any particular τ will not necessarily be the equilibrium value of $f = (1 + k_1/k_2)^{-1}$. This is because τ might not be long enough for sufficient time averaging to occur (*i.e.*, to invoke ergodicity). Instead, each τ will exhibit a distinct, time-averaged value of f.

The exact value of f for a particular τ will depend upon the molecule's stochastic path through state-space during τ. As such, a probabilistic description of f, which accounts for all possible paths through state-space, is needed to describe the likelihood of observing a particular value of f during a τ (22). In particular, for the reversible, two-state system considered here, such a description, which has roots in the analysis of the NMR chemical exchange effects described above (23) and in sojourn-time probability distributions (24), was first given by Dobrushin (25). This particular expression (derived in the *Supporting Information*) is a function of k_1, k_2, and τ, and has been used in many single-molecule studies—though mostly in the context of photon counting experiments and without Bayesian inference-based implementations (16–26). Experimentally, if the exact values of f, ϵ_1, and ϵ_2 during each τ were known, one would be able to calculate the expected value of the corresponding time-averaged signal, μ, for each τ, because it would be the linear combination $\mu = f\epsilon_1 + (1-f)\epsilon_2$. Unfortunately, the analysis of time-resolved, single-molecule experiments deals with the opposite problem—observing a signal value, *d*, during each τ and trying to infer f, ϵ_1, and ϵ_2.

Generally, the values of *d* that are recorded during each τ are random variables, which are distributed according to a probability distribution function (PDF). For any number of states, this PDF for the observed values of *d* is the convolution of the PDFs for the signal values associated with each individual state, weighted by the fraction of time spent in that state (*i.e.*, $d \sim f_1 p(\epsilon_1) * \ldots * f_n p(\epsilon_n)$, where f_i is the fractional occupancy of the i$^{\text{th}}$ state, $p(\epsilon_i)$ is the PDF of the signal values associated with the i$^{\text{th}}$ state, and $*$ denotes a convolution). For many experimental techniques, the signal values associated with each state are, or are approximately, distributed according to a normal PDF (*i.e.*, a Gaussian) with mean ϵ_i and variance σ_i^2 for the i$^{\text{th}}$ state. Because the convolution of two normal PDFs is another normal PDF, in this case the PDF for the observed values of *d* is a normal distribution with mean $\mu = \sum_i f_i \epsilon_i$ and variance $\sigma^2 = \sum_i f_i \sigma_i^2$. Furthermore, we can also account for noise from the detection process (*e.g.*, a normal PDF with mean 0 and variance σ_{noise}^2), as well as a time-

dependent baseline (*e.g.,* baseline drift at time t, b_t, that is driven by white-noise is a normal PDF with mean b_{t-1} and variance σ^2_{drift}) through additional convolutions; in these examples, the resulting PDF of *d* is again a normal PDF with mean $\mu = \mathrm{b}_{t-1} + \sum_i f_i \epsilon_i$ and variance $\sigma^2 = \sigma^2_{drift} + \sigma^2_{noise} + \sum_i f_i \sigma_i^2$. Unfortunately, since μ and σ depend upon the set of fractional occupancies, $\{f\}$, which are not experimental observables, we have no way of knowing the exact form of this PDF—information that is required to calculate the probability of observing a particular value of *d*.

To circumvent this experimental limitation, the dependence of the PDF upon $\{f\}$ can be removed by marginalizing $\{f\}$ out of the expression for the PDF that was described above. This marginalized probability distribution of *d* then describes the likelihood of experimentally observing a particular value of *d* during a τ as a function of the set of rate constants for transitions between the states, $\{k\}$, the set of signal values corresponding to those states, $\{\epsilon\}$, and the set of the amounts of noise in those states, $\{\sigma\}$, regardless of the exact values of $\{f\}$ (Fig. 1A). As expected from the discussion in the previous section, this expression describes effects similar to those of chemical exchange in NMR experiments, in which rates with which nuclei exchange that are larger than the resonance frequency difference between exchanging nuclei cause distinct resonances to coalesce into a single, averaged resonance. As shown in Fig. 1B for a two-state system (see *Supporting Information* Eqn. 10), the effect of increasing rate constants k_1 and k_2 results in distinct signal peaks centered at ϵ_1 and ϵ_2 to coalesce into a single, averaged peak centered at $\langle\epsilon\rangle$.

With such an expression describing the marginalized probability distribution of *d* we can then use Bayesian inference to estimate the parameters governing the single-molecule system (*i.e.*, $\{\epsilon\}$, $\{\sigma\}$, and $\{k\}$) from the series of the *d* that comprise each of the signal trajectories. Primarily due to recent developments in computational tractability, Bayesian inference has become a powerful method for the analysis of biophysical data, such as determining the phases of X-ray reflections in X-ray crystallographic studies (27), performing simultaneous phylogenetic analysis of nucleotide and protein datasets (28), elucidating the number of structural classes present in cryogenic electron microscopy images (29), and ascertaining the number of states and the rates of transitions between those states present in single-molecule signal trajectories (30, 31). For an introduction to Bayesian inference, see Refs. 6, 7, 32, and the *Supporting Information*.

Unfortunately, performing Bayesian inference on a multi-parameter system, such as the one described here, results in a multi-dimensional, joint-probability distribution of the model parameters known as a posterior probability distribution, which is difficult to evaluate (32). In order to overcome this difficulty, we have chosen to evaluate the posterior probability distribution of the model parameters by numerically sampling it using a Markov chain Monte Carlo (MCMC) (6, 33) method with affine-invariant ensemble sampling (34, 35). Although alternative methods that approximate the posterior probability distribution of the model parameters, such as the Laplace approximation or variational inference, might be more computationally tractable, MCMC sampling is advantageous in that, unlike such approximation methods, it can provide an exact result that does not assume a particular structure of the posterior probability distribution (6). Regardless of the choice of method, however, the most important aspect of the approach described here is that we can evaluate the posterior probability distribution of the model parameters from the series of *d* that comprise a single-molecule signal trajectory in a manner that completely accounts for the time resolution of the experimental technique.

Results and Discussion

Analysis of Computer-Simulated Single-Molecule Signal Trajectories Reporting on the Kinetics of a Ligand Binding and Dissociation Process

To demonstrate the use of the analytical formulas underlying BIASD, we analyzed simulated single-molecule signal trajectories that mimic the binding and dissociation of a ligand to its target biomolecule, a receptor, using the two-state, reversible kinetic scheme discussed in the previous section (36). In this example, ϵ_1 and ϵ_2 represent the signal values of the receptor in the ligand-free state and the ligand-bound state, respectively, and σ represents the standard deviation of the signal values for both states. Correspondingly, k_1 and k_2 represent the pseudo-first-order rate constant of ligand binding to the receptor, and the first-order rate constant of ligand dissociation from the receptor, respectively. As such, k_1 is dependent on $[L]$ with a dependence that is given by $k_1 = k_1^* \cdot [L]$, where k_1^* is the second-order rate constant for binding of the ligand to the receptor and $[L]$ is the ligand concentration, and k_2 is not dependent on $[L]$. In order to emulate a titration experiment, we varied the $[L]$ to alter the fraction of ligand-bound receptor from ~0.1% to ~99.9% and simulated a series of individual signal trajectories where the $[L]$ spanned six decades centered around the $[L]$ corresponding to the equilibrium dissociation constant, $[L] = K_D$. Notably, as is always the case for experimentally recorded signal trajectories, the finite length of each simulated signal trajectory presents an intrinsic limit to the amount of kinetic information contained in each signal trajectory. Finally, estimates of the parameters that were used to simulate the signal trajectories were obtained by analyzing the simulated signal trajectories using two idealization-based approaches: (i) half-amplitude signal thresholding (13) followed by Bayesian inference to infer the transition probability and quantify the kinetics (2) (Bayesian threshold), and (ii) an HMM (6) that used the maximum-likelihood framework to estimate the transition probability and quantify the kinetics (ML HMM). In addition to these two idealization-based approaches, the simulated signal trajectories were also analyzed using the BIASD approach presented here.

As shown in Figure 2A, the values of k_1 and k_2 obtained using both idealization approaches are inaccurate (green and red curves, respectively). Interestingly, however, neither approach absolutely outperforms the other in accuracy, and both plateau at the acquisition rate (*i.e.*, τ^{-1} = 10 s^{-1}). Notably, the use of Bayesian inference in the Bayesian threshold approach tempers the fluctuations that are seen in the rate constants obtained from the ML HMM at high $[L]$. These fluctuations originate from the maximum likelihood framework used to estimate the transition probability in the ML HMM approach. Tempering of these fluctuations in the Bayesian threshold approach results from the use of a prior probability distribution, which describes the initial knowledge of the model parameters, in Bayesian inference (2, 6). Regardless, the rate constants were systematically underestimated across nearly the entire range of $[L]$s that were simulated, and this underestimation worsens with increasing $[L]$. It is striking that the values of k_1 and k_2 obtained using the Bayesian threshold idealization are also relatively precise—a misleading consequence of using idealization methods in general (2).

With regard to the values of ϵ_1 and ϵ_2 obtained using both idealization approaches, Figure 2B demonstrates that, while these methods can accurately determine the value of ϵ_1 if the receptor preferentially occupies the ligand-free state (low $[L]$) or ϵ_2 if the receptor preferentially occupies the ligand-bound state (high $[L]$), the time averaging caused by large values of k_1 shift the inferred values of ϵ_1, sometimes quite significantly, toward the simulated value of ϵ_2, and *vice versa*. Here, the Bayesian threshold approach provided more accurate estimates of ϵ_1 and ϵ_2 than did the ML HMM. However, this was only because the signal threshold was set halfway between ϵ_1 and ϵ_2 using the known simulation parameters, thereby optimally minimizing the misclassification of states 1 and 2, and, consequently, maximizing the accuracy with which ϵ_1 and ϵ_2 are estimated; this is also why the estimates of σ from the Bayesian threshold approach are more accurate than those from the ML HMM (Fig. 2C) (13).

In contrast to both idealization approaches, the values of k_1 and k_2 obtained using BIASD are highly accurate (Fig. 2A). The simulated values of k_1 and k_2 are well encompassed by the 95% credible interval of the posterior probability distribution across the entire range of $[L]$s that were simulated, which includes rate constants that are up to three orders of magnitude larger than the simulated time resolution. In addition, the values of k_1 and k_2 are highly precise, as the 95% credible intervals of the posterior probability distribution are strikingly narrow over a range of $[L]$s corresponding to a value of k_1 that is over an order of magnitude smaller than τ^{-1} to one that is over an order of magnitude larger than τ^{-1}. Importantly, as the amount of data that is analyzed increases, the contribution that the choice of prior probability distribution (*i.e.*, the initial knowledge of k_1, k_2, ϵ_1, ϵ_2, and σ) makes to the posterior probability distribution diminishes. Consistent with the amount of data that are typically analyzed in single-molecule biophysical experiments, the results reported here are relatively insensitive to the prior probability distributions used for the analysis.

At the lower $[L]$s, the broadening of the posterior probability distribution that limits the precision for the estimates of k_1 and k_2 in both BIASD as well as the Bayesian threshold idealization arises from the finite amount of information regarding k_2 and ϵ_2 that is contained in signal trajectories that exhibit very low occupation of the ligand-bound state of the receptor. Likewise, at the higher $[L]$s, the broadening of the posterior probability distribution, and the implied limitations to the precision for estimating k_1 and k_2 that is observed, arises from the finite amount of information regarding k_1 and ϵ_1 that is contained in signal trajectories that exhibit very low occupation of the ligand-free state of the receptor. In this analysis, the prior probability distribution limits the 95% credible interval of the posterior probability distribution for k_1 and k_2 from continually expanding with increasing $[L]$. Regardless, the uncertainty at the lower and higher $[L]$s is a consequence of the finite amount of information in a finite-length signal trajectory, as many reciprocal pairs of k_1 and ϵ_1 values (*i.e.,* a larger k_1 and a smaller ϵ_1 or a smaller k_1 and a larger ϵ_1) are consistent with the data. In an experimental situation, this imprecision can be alleviated by employing prior probability distributions for the $\{\epsilon\}$ values using the results of experiments performed under conditions in which one state is preferentially occupied, for instance, the values of ϵ observed in the absence of ligand could be used to construct a prior probability distribution for the values of ϵ associated with the ligand-free state of the receptor, whereas the values of ϵ observed in the presence of saturating $[L]$ could be used to construct a prior probability distribution for the values of ϵ associated with the ligand-free state of the receptor. In the case of large-scale conformational rearrangements, one could similarly use a buffer condition, ligand, temperature, or mutation that preferentially stabilizes one state, or, alternatively, one could use molecular structures or models to estimate prior probability distributions of $\{\epsilon\}$ values. With regard to the values of ϵ_1 and ϵ_2 obtained using BIASD, Figure 2B demonstrates that these values were accurately inferred regardless of the value of $[L]$, even at $[L]$s at which the idealization approaches drastically misestimate them. Finally, unlike the idealization approaches, which were only able to successfully infer σ when the signal trajectories were almost entirely in the ligand-bound- or ligand-free states, BIASD was also able to accurately and precisely infer σ from the simulated signal trajectories with intermediate values of $[L]$ (Fig. 2C).

In summary, we were able to use BIASD to obtain accurate and precise posterior probability distributions for k_1, k_2, ϵ_1, ϵ_2, and σ across the entire range of $[L]$s that were simulated. Notably, BIASD was even successful when the rate constants in the simulated, single-molecule signal trajectories were much smaller then τ^{-1}, although we note that, in this regime, the conventional analysis of idealizing the signal trajectories is much more computationally efficient. Most importantly, BIASD was able to accurately and precisely infer the rates constants and the signal values for simulated, single-molecule signal trajectories in which the rate constants were up to three orders of magnitude larger than τ^{-1}, and up to about four orders of

magnitude larger than the τ^{-1}s where conventional idealization of signal trajectories begins to yield significant errors in the rate constants.

Analysis of Experimentally Observed Single-Molecule E_{FRET} Trajectories Reporting on the Kinetics of a Large-Scale Conformational Rearrangement

To demonstrate the use of BIASD in the analysis of experimental data, we chose to analyze experimentally observed, single-molecule E_{FRET} trajectories reporting on a large-scale conformational rearrangement of the ribosome. This essential, two-subunit, ribonucleoprotein-based, biomolecular machine is universally responsible for the translation of messenger RNAs (mRNAs) into proteins in living cells. The ribosome synthesizes proteins by repeatedly incorporating amino acids, delivered in the form of aminoacyl-transfer RNA (tRNA) substrates, into a nascent polypeptide chain in the order dictated by the mRNA being translated. During the elongation stage of protein synthesis (37), the ribosomal pre-translocation (PRE) complex undergoes stochastic, thermally driven fluctuations between two major, on-pathway conformational states that we refer to as global state 1 (GS1) and global state 2 (GS2), defining a dynamic equilibrium, GS1⇌GS2 (38, 39). These transitions between GS1 and GS2 constitute large-scale rearrangements of the PRE complex that involve relative rotations of the ribosomal subunits, reconfigurations of the ribosome-bound tRNAs, and repositioning of a ribosomal structural domain known as the L1 stalk (Fig. 3A) (40).

Previously, we have conducted wide-field microscopy smFRET studies of the temperature dependence of the rate constants governing GS1→GS2 and GS2→GS1 transitions by imaging a Cy3 FRET donor fluorophore- and Cy5 FRET acceptor fluorophore-labeled PRE complex analog lacking a tRNA at the ribosomal aminoacyl-tRNA binding (A) site (PRE^{-A}) in a temperature-controlled, microfluidic observation flowcell (9). Unfortunately, the increase in thermal energy that accompanied the increasing temperature caused the rate constants for the transitions between GS1 and GS2 to increase such that, at the highest temperatures, the E_{FRET} trajectories contained a significant number of time-averaged data points (Fig. S1). Regrettably, the time averaging in these E_{FRET} trajectories precluded accurate determination of the rate constants, and, correspondingly, an analysis of the thermodynamic properties of the transition-state energy barriers that control the GS1→GS2 and GS2→GS1 conformational rearrangements (9). To overcome these limitations, we have used BIASD to analyze the sets of E_{FRET} trajectories of PRE^{-A} complexes that we have previously collected at 22, 25, 28, 31, 34, and 37 °C (9). Here, we assume that the GS1⇌GS2 equilibrium can be represented by a single, reversible two-state kinetic scheme (Fig. 3A). In this kinetic scheme, k_{GS1} and k_{GS2} represent the unimolecular rate constants for the GS1→GS2 and GS2→GS1 conformational rearrangements, respectively. Correspondingly, ϵ_{GS1} and ϵ_{GS2} represent the E_{FRET} values of GS1 and GS2, respectively.

These six sets of E_{FRET} trajectories were analyzed using BIASD to provide estimates of k_{GS1}, k_{GS2}, ϵ_{GS1}, ϵ_{GS2}, and σ that describe the set of E_{FRET} trajectories observed at each temperature. The values of k_{GS1} and k_{GS2} that were inferred using BIASD increase with temperature (Fig. 3B), and, at the highest temperatures, were greater than 1/10th of τ^{-1} – the regime where idealization approaches begin to systematically underestimate rate constants. We note that although the values of k_{GS1} and k_{GS2} inferred using BIASD are those that best describe the entire set of E_{FRET} trajectories observed at a particular temperature, individual E_{FRET} trajectories at each temperature are consistent with rate constants > 45 s^{-1}, while others are consistent with rate constants < 0.1 s^{-1}. This broad range of kinetic behaviors suggests the possibility that the PRE^{-A} complexes are compositionally heterogeneous (*e.g.*, sub-populations of PRE^{-A} complexes that differ in the aminoacylation status of the tRNA at the ribosomal peptidyl-tRNA binding (P) site, the presence or absence of a tRNA at the ribosomal tRNA exit (E) site, and/or the presence or absence of a particular ribosomal protein)

and/or are conformationally heterogeneous due to structural rearrangements that are slow on the time-scale of the experiment and effect k_{GS1} and k_{GS2}, but not necessarily ϵ_{GS1} and ϵ_{GS2}. Additionally, we note that the posterior probability distributions of ϵ_{GS1} and ϵ_{GS2} that were inferred using BIASD have means of 0.13 and 0.78, respectively, which are values of ϵ_{GS1} and ϵ_{GS2} that very closely match the values of the mean E_{FRET} of GS1 and GS2 reported in previous, room-temperature studies of the analogous PRE^{-A} complex (0.16 and 0.76, respectively) (41). This correspondence strongly suggests that the values of ϵ_{GS1} and ϵ_{GS2} inferred using BIASD are accurate, regardless of the presence of time averaging in the E_{FRET} trajectories recorded at the highest temperatures.

With the inferred values of k_{GS1} and k_{GS2} as a function of temperature, we then used transition-state theory to quantify the apparent transition-state energy barriers along the apparent GS1→GS2 and GS2→GS1 reaction coordinates (42–45). Kramers' barrier-crossing theory, which was developed to analyze thermally activated, condensed-phase transitions of a Brownian particle (43–45) and is increasingly being used to analyze the conformational dynamics and folding of small, globular proteins (12, 46), may ultimately provide a more exact analysis of the apparent transition-state energy barriers along the apparent GS1→GS2 and GS2→GS1 reaction coordinates. However, its application requires knowledge regarding the viscosity of the aqueous buffer in which the PRE^{-A} complex is dissolved and the 'internal friction' of the PRE^{-A} complex that are unavailable in the current study (12, 47). As such, we have opted to use transition-state theory, and regard the results as upper limits on the apparent transition-state energy barriers along the apparent GS1→GS2 and GS2→GS1 reaction coordinates, which do not account for internal friction or transition-state recrossings. To apply transition-state theory, we used the marginalized posterior probability distributions of the rate constants at each temperature to infer $\Delta H^{\ddagger}$ and $\Delta S^{\ddagger}$ from the equation $k_{TST} = \kappa k_B T/h\, exp(-(\Delta H^{\ddagger} - T\Delta S^{\ddagger})/(k_B T))$, where κ is the transmission coefficient and is taken to be unity, k_B is the Boltzman constant, h is Planck's constant, and $\Delta H^{\ddagger}$ and $\Delta S^{\ddagger}$ are the enthalpic and entropic differences between the transition and ground states (Fig. 3B). The marginalized results for the GS1→GS2 transition are $\Delta H^{\ddagger}_{GS1}$ = 11.3 (7.9, 15.0) kcal mol^{-1} and $\Delta S^{\ddagger}_{GS1}$ = –20.1 (-31.3, -8.1) cal mol^{-1} K^{-1}, and for the GS2→GS1 transition are $\Delta H^{\ddagger}_{GS2}$ = 10.3 (8.1, 12.7) kcal mol^{-1} and $\Delta S^{\ddagger}_{GS2}$ = –22.7 (-29.9, -15.0) cal mol^{-1} K^{-1}, where the numbers in parenthesis represent the lower and upper bounds for the 95% credible interval. Notably, the posterior probability distributions for $\Delta H^{\ddagger}$ and $\Delta S^{\ddagger}$ are highly correlated such that across all of the temperatures measured here, $\Delta G^{\ddagger}_{GS1}$ and $\Delta G^{\ddagger}_{GS2}$were sufficiently resolved; for instance, at 37 °C, $\Delta G^{\ddagger}_{GS1}$ = 17.57 (17.50, 17.65) kcal mol^{-1}, and $\Delta G^{\ddagger}_{GS2}$ = 17.34 (17.29, 17.39) kcal mol^{-1}. Unfortunately, a structure-based interpretation of the absolute $\Delta H^{\ddagger}$ and $\Delta S^{\ddagger}$ values for the GS1→GS2 and GS2→GS1 transitions of a single PRE^{-A} complex is significantly complicated by the complexity of the enthalpic and entropic changes that are associated with conformational rearrangements of large macromolecular complexes, and by the inherent limitations of transition-state theory (5, 42, 48). Nonetheless, structure-based interpretations of the relative changes of the $\Delta H^{\ddagger}$s and $\Delta S^{\ddagger}$s ($\Delta\Delta H^{\ddagger}$s and $\Delta\Delta S^{\ddagger}$s) between different pairs of PRE^{-A} complexes (*e.g.*, containing different tRNAs at the peptidyl-tRNA binding (P) site, containing wildtype or mutant P-site tRNAs, consisting of wildtype or mutant ribosomes, *etc.*) are much more straightforward and can reveal the thermodynamic contributions that particular structural features of tRNAs or ribosomes make to the apparent transition-state energy barriers along the apparent GS1→GS2 and GS2→GS1 reaction coordinates. Combined with the temperature-controlled, single-molecule microscopy platform that we have previously described (9), the analytical framework presented in this section now enables the collection, analysis, and interpretation of such data.

Inferring rate constants and signal values from systems with sub-populations of molecular properties

BIASD can be extended to address the presence of multiple, time-averaged sub-populations of molecular properties. These sub-populations may be static or interconvert, and may be present in an individual molecule or found among an ensemble of molecules. In such a situation, we can classify each data point as belonging to one of K different types of time-averaged sub-populations, and then use a '1-of-K' vector, $\vec{z}_{ij}$, to denote to which of the K sub-populations the ith data point from the jth molecule belongs. Given the one particular sub-population specified by $\vec{z}_{ij}$, the likelihood of this data point being described by the parameters of this sub-population is calculated as described above for the case of the time-averaged, single-population system. Unfortunately, in an experimental situation there is no way of knowing which sub-population a particular data point belongs to, thereby preventing the likelihood of this data point from being evaluated; this situation is similar to that of the unknown fractional occupancy, f, described above.

To address this shortcoming, we could try to infer the values of all the $\vec{z}_{ij}$ along with all of the other BIASD model parameters, but this is an unreasonable number of variables for an inference procedure. Additionally, we are often not concerned with the exact values of $\vec{z}_{ij}$, so much as with the occupancies of the K states (*e.g.*, the steady-state occupation probabilities) or with the rate constants that describe transitions between the K states. Fortunately, instead of performing inference to learn the model parameters and the set of $\vec{z}_{ij}$s, $\{\vec{z}_{ij}\}$, we can marginalize out all of the $\{\vec{z}_{ij}\}$ with the expressions for the probability of each $\vec{z}_{ij}$. For instance, in the case of a mixture of static sub-populations of molecular properties among an ensemble of molecules (*e.g.*, a mixture of post-transcriptionally or post-translationally modified and unmodified molecules within an ensemble), these probabilities would be time-independent variables that specify the fraction of each sub-population of the ensemble; this approach is called a mixture model. Marginalization would then involve summing the likelihoods for the different sub-populations, weighted by the probabilities of those sub-populations. Consequently, during the inference procedure, the probabilities of the sub-population occupancies would then become model parameters that are also inferred using Bayes' rule.

Additionally, it is possible to have a time-dependent system with hierarchical transitions between the different sub-populations. In this case, the probabilities of each $\vec{z}_{ij}$ in the $\{\vec{z}_{ij}\}$ would not be constant for each sub-population, as they would be for a mixture model, but would instead depend upon the sub-population of the previous data point $\vec{z}_{i-1,j}$ and a K x K transition matrix, $\mathbf{A}_{ij} = e^{\mathbf{Q}t_{ij}}$, where $\mathbf{Q}$ is the rate matrix that depends upon the set of rate constants for transitioning between the K different states, and t_{ij} is the time that has elapsed since the previous data point, which may not necessarily be equal to τ (Fig. 1C). Here, marginalization is efficiently performed with the forward-backward algorithm (49) and the steady-state probabilities, as calculated from the rate constants for the kinetic scheme under consideration, for instance by using the diagram method (50), are used to set the initial probability of each $\vec{z}_{0j}$. In total, this approach amounts to a hierarchical, continuous-time, ensemble HMM for sub-temporal resolution systems, where inference is performed directly upon the rate constants, instead of the transition probabilities. Consequently, this approach can handle shuttering of the laser light source in fluorescence microscopy experiments or other types of irregular spacing of data points, sub-temporal resolution data, and population-level analyses with non-parametric posterior distributions, which can be used to ascertain the underlying thermodynamic landscape of the mesoscopic ensemble.

To highlight this hierarchical approach, consider a single-molecule fluorescence microscopy experiment in which a fluorophore-labeled biomolecule transitions between two states, 1 and 2, with forward and reverse rate constants k_{12} and k_{21}, respectively (Fig. 4A). Unfortunately, such fluorescence microscopy experiments often suffer from photophysical phenomena such as fluorophore photoblinking, in which a fluorophore temporarily transitions into a long-lived, 'dark', excited molecular electronic state and thus transiently stops fluorescing, or fluorophore photobleaching, in which a fluorophore that has transitioned into an excited molecular electronic state undergoes a photochemical reaction and permanently stops fluorescing (51). Often, the transition rates into and out of the dark states responsible for photoblinking are faster than the time resolution of techniques such as wide-field, fluorescence microscopy. As a result, instead of detecting a steady level of fluorescence intensity from the fluorophore, sub-temporal-resolution transitions between fluorescent and dark states of the fluorophore manifests as an extra, and often dominant, source of 'noise' in the single-molecule fluorescence intensity signal trajectory (Fig. 4B, inset). Intense experimental effort has gone into minimizing these photophysical effects, including the use of fluorophores, such as Cy3B, that have been chemically altered so as to minimize transitions to dark states (52); elaborate excitation laser modulation schemes, such as triplet-state relaxation (T-Rex) and dark-state relaxation (D-Rex) schemes, that minimize transitions to higher-order dark states (53, 54); photostabilizing additives, such as Trolox, that accelerate transitions out of dark states (55, 56); and fluorophore-photostabilizer conjugates, such as Cy3- and Cy5-triplet state quencher conjugates, that accelerate transitions out of dark states (57, 58). Here, we show how extending BIASD with the hierarchical HMM described above allows us to computationally overcome these photophysical effects.

To demonstrate this ability, we simulated the kinetic scheme shown in Fig. 4A, where a fluorophore-labeled biomolecule transitions between conformational states 1 and 2 with signal values of ϵ_1 and ϵ_2, respectively. However, in this simulation, both of these states can rapidly transition into and out of a photoblinked state, denoted 0 with signal value $\epsilon_0 = 0$, at rates much faster than the time resolution of the simulated data. These dynamics continue until the system eventually transitions into a photobleached state, denoted Ø with signal value $\epsilon_{\emptyset} = 0$. A similar situation has been recently investigated by Chung *et al.* to analyze FRET photon trajectories reporting on the sub-temporal resolution folding and unfolding dynamics and photoblinking dynamics of the villin subdomain protein (20). As expected, by analyzing this simulation using this hierarchical approach, the posterior probability distribution of the parameters describing the fluorescence emission from each sub-population (ϵ_1, ϵ_2, σ, k_{10}, k_{01}, k_{20}, and k_{02}; see Fig. 1C), as well as the rate constants describing the transitions between states 1 and 2 (k_{12}, and k_{21}; see Fig. 4A), were all found both accurately and precisely as the parameter values used for the simulation fall within the inferred 95% credible intervals (Fig. S2). To provide visual intuition into this result, we also have shown the Viterbi-idealized path from the maximum *a posteriori* (MAP) estimate of the model parameters in order to show the most likely fluorescence intensity signal trajectory in the absence of photoblinking (Fig. 4B). Detection noise from the marginalized posterior distribution of σ was added to this path to show what the data might have looked like in the absence of photoblinking. Regardless, we note that this particular path is essentially a point estimate of the $\{\vec{z}_{ij}\}$, whereas, by marginalizing out all of the $\{\vec{z}_{ij}\}$ during the inference procedure, we have actually considered all the other possible paths, regardless if a transition is missed in the Viterbi path. As such, the posterior probability distribution of the model parameters is a more encompassing result (Fig. S2). Finally, we note that the hierarchical HMM treatment that we present here is general and applicable to not just two, but to any number of K sub-populations.

Conclusion

By analyzing the fraction of time that a single-molecule spends in each state of a defined kinetic scheme during each τ in a signal trajectory, BIASD adopts a fundamentally different approach to the analysis of time-resolved, single-molecule experiments than that which has been traditionally employed by methods that idealize the trajectories (*e.g.*, signal thresholding, HMMs, *etc.*). Using computer-simulated and experimentally observed data, we have demonstrated that this powerful approach enables BIASD to accurately and precisely infer the rate constants of a two-state kinetic scheme as well as the signal values corresponding to these two states, even when the rates of transitions between the states are orders of magnitude larger than the time resolution of the signal trajectories. When used to analyze experimental E_{FRET} trajectories reporting on the dynamics of single PRE^{-A} complexes recorded as a function of temperature (9), BIASD allowed us to infer the thermodynamic activation parameters characterizing the transition-state energy barriers along the GS1→GS2 and GS2→GS1 reaction coordinates, which had thus far remained inaccessible to traditional smFRET data analysis approaches. Moreover, we have demonstrated that a straightforward extension of the BIASD framework enables the kinetics of experimental systems exhibiting multiple sub-populations of molecular properties to be accurately and precisely inferred.

It is important to note that the BIASD framework is general and can be applied to any experimentally observed signal trajectory that exhibits stochastic transitions between distinct states, regardless of the nature or the origin of the signal. Thus, BIASD can be used to temporally resolve data collected using virtually any time-resolved single-molecule experimental method, including single-molecule fluorescence microscopy, force spectroscopy, conductance, and tethered particle motion methods. Moreover, although here we have developed BIASD to analyze single-molecule signal trajectories, we have not consider the temporal ordering of the data. Consequently, in addition to analyzing individual single-molecule signal trajectories, BIASD can also be used to analyze the distribution of fractional occupancies observed across an entire ensemble of individual molecules during a given τ. This could allow non-equilibrium phenomenon to be monitored across an ensemble of single molecules, time period by time period (*e.g.*, stopped-flow delivery of a ligand, substrate, cofactor, or inhibitor to an enzyme or other biomolecule). In addition, BIASD can be expanded to include the time evolution of the state occupation probabilities (*c.f.,* Eqn. 2 of the *Supporting Information*), or to incorporate time dependence into the model parameters $\{k\}$, $\{\epsilon\}$, and $\{\sigma\}$ (*e.g.*, the varying of $\{\epsilon\}$ in single-molecule particle tracking experiments).

Regarding the performance of BIASD on experimental data, we note that the rate constants and signal values of a system can be more precisely inferred from experiments that collect higher SNR data, because then there is less uncertainty in the time-averaged fractional occupancies of the signal trajectories. Therefore, somewhat counterintuitively, sub-temporal-resolution dynamics can to some degree be more precisely inferred from signal trajectories recorded with lower time resolutions but higher SNRs (*e.g.,* due to better photon conversion efficiencies on an electron-multiplying charge-coupled device), than those recorded with higher time resolutions but lower SNRs. Additionally, although we have focused the current work on the most widely applicable case of a Markovian, two-state system in which the noise of the signal can be modeled using a normal distribution, the Bayesian inference-based framework underlying BIASD can be readily extended to non-Markovian dynamics (21, 59), N-state kinetic schemes (60, 61), or systems in which the noise of the signal can be modeled using distributions other than a Normal distribution (18, 62). It should be noted, however, that such developments will come with added computational expenses. To facilitate the analysis of single-molecule data using BIASD, as well as to enable the future extension of BIASD along the lines described here, we have

made the BIASD source code available at https://github.com/ckinzthompson/biasd. The source code is written in Python and integrated with computationally intensive functions provided in C as well as in CUDA (for GPU-based computation) in order to balance accessibility with high-performance.

Methods

Simulating Signal Trajectories

State trajectories were simulated with the stochastic simulation algorithm (36); briefly, sequential random lifetimes were drawn from exponential distributions with the specified rate constants, and subsequent states were chosen randomly according to the splitting probabilities. A random starting point for the initiation of the trajectory (t = 0 sec) was selected with a uniform distribution from the first lifetime. The fractional occupancies of each state during each sequential τ were then calculated from the sequence of lifetimes. The resulting fractional occupation *versus* time trajectories were turned into signal trajectories by computing μ, and then adding normally distributed noise with standard deviation, σ.

Bayesian Thresholding Analysis

Signal trajectories were idealized by thresholding any measurement period with signal less than $(\epsilon_1 + \epsilon_2)/2 = 0.5$ into state 1, and otherwise into state 2. Rate constants from the ith state to jth state were then calculated as $k_{ij} = -\ln(1 - p_{ij})/\tau$ where p_{ij} is the transition matrix from the idealized trajectory (2). Credible intervals for the transition probabilities, and rate constants were calculated with uniform prior distributions (2). The joint posterior probability distributions of ϵ_1 and $1/\sigma_1^2$, and ϵ_2 and $1/\sigma_2^2$ were inferred using the analytical formulas for Bayesian inference with a joint normal-gamma prior probability distribution using those data points that were idealized into the respective states (6). The marginalized posterior distributions of the ϵ_i and $1/\sigma_i^2$ (T and gamma distributions, respectively) were used to calculate means and 95% credible intervals for each parameter (6). An aggregate σ was then calculated by weighting σ_1^2 and σ_2^2 by the fraction of data points idealized into each state and taking the square root of their sum.

Maximum Likelihood HMM Analysis

Signal trajectories were analyzed using a two-state, discrete, maximum likelihood HMM with normal distribution emissions using the expectation maximization, and forward-backward algorithms (6, 49). Each trajectory was analyzed with 20 randomized restarts, including one initialized at the simulated values, until the likelihood of each restart converged to a relative value of 10^{-10}. From these, the point-estimate with the greatest likelihood was used in subsequent analyses. Rate constants were calculated directly from the transition probability matrix point-estimate, and an aggregate standard deviation was calculated as described above for Bayesian thresholding.

BIASD Analysis

Adaptive, Gauss-Kronrod (G10, K21) quadrature was used to numerically integrate the BIASD likelihood function on an Nvidia GeForce 1080 GTX graphics card; the likelihood of each data point took about 1 µsec to compute. The posterior probability distribution was sampled using *emcee*, an ensemble, affine-invariant MCMC method (34, 35). For each trajectory, 100 MCMC walkers were employed to draw 2000 samples each, and the first 1000 samples were discarded to burn in the chain. From the remaining samples, independent samples were chosen spaced apart by the maximum parameter autocorrelation time, and credible intervals and means were calculated from these samples.

PRE^{-A} E_{FRET} Analysis

Previously published Cy3 and Cy5 fluorescence intensity, I_{Cy3} and I_{Cy5}, *versus* time trajectories from the PRE^{-A} complex from the study by Wang and coworkers (9) were transformed into E_{FRET} trajectories by calculating $E_{FRET} = I_{Cy5}/(I_{Cy3} + I_{Cy5})$ at each measurement period. Outliers where $E_{FRET} < -0.4$ or $E_{FRET} > 1.4$ were clipped. The number of E_{FRET} trajectories in the 22, 25, 28, 31, 34, and 37 °C datasets were 490, 456, 435, 452, 270, and 459, respectively. Uniform distributions were used for the prior probability distributions. The first and second moments, $E[k]$ and $E[k^2]$, of the marginalized posterior probability distributions for k_{GS1} or k_{GS2} were used to infer the values of $\Delta H^{\ddagger}$, $\Delta S^{\ddagger}$, and a precision λ using Bayesian inference with the likelihood function $p\left(\{E[k_i], E[k_i^2]\}|\Delta H^{\ddagger}, \Delta S^{\ddagger}, \lambda, \{T_i\}\right) = \prod_i \mathcal{N}\left(E[k_i]|\mu = k_{TST}\left(\Delta H^{\ddagger}, \Delta S^{\ddagger}, T_i\right), \Sigma = \lambda^{-1} + \left(E[k_i^2] - E[k_i]^2\right)\right)$, where $\mathcal{N}$ is the normal distribution with mean μ and variance Σ, where $k_{TST}\left(\Delta H^{\ddagger}, \Delta S^{\ddagger}, T_i\right)$ is the rate constant calculated at temperature T_i with transition state theory, and where i indexes the set of temperatures. The resulting posterior probability distribution for $\Delta H^{\ddagger}$, $\Delta S^{\ddagger}$, and λ was sampled using MCMC from which credible intervals and means were calculated.

References

1. Tinoco I, Gonzalez RL (2011) Biological mechanisms, one molecule at a time. *Genes Dev* 25(12):1205–1231.
2. Kinz-Thompson CD, Bailey NA, Gonzalez RL (2016) Precisely and Accurately Inferring Single-Molecule Rate Constants. *Methods in Enzymology*, pp 187–225.
3. Cavanagh J, Fairbrother WJ, Palmer, III AG, Skelton NJ (1996) *Protein NMR Spectroscopy: Principles and Practice* (Academic Press, Inc., San Diego).
4. Boehr DD, Dyson HJ, Wright PE (2006) An NMR perspective on enzyme dynamics. *Chem Rev* 106(8):3055–3079.
5. McCammon JA (1984) Protein dynamics. *Reports Prog Phys* 47(1):1–46.
6. Bishop CM (2006) *Pattern Recognition and Machine Learning* (Springer, New York).
7. Jaynes ET (2003) *Probability Theory: The Logic of Science* (Cambridge University Press, Cambridge).
8. Bretthorst GL, Hung CC, D'Avignon DA, Ackerman JJH (1988) Bayesian analysis of time-domain magnetic resonance signals. *J Magn Reson* 79(2):369–376.
9. Wang B, Ho J, Fei J, Gonzalez RL, Lin Q (2011) A microfluidic approach for investigating the temperature dependence of biomolecular activity with single-molecule resolution. *Lab Chip* 11(2):274–81.
10. Fenimore PW, Frauenfelder H, McMahon BH, Parak FG (2002) Slaving: solvent fluctuations dominate protein dynamics and functions. *Proc Natl Acad Sci* 99(25):16047–16051.
11. Lubchenko V, Wolynes PG, Frauenfelder H (2005) Mosaic energy landscapes of liquids and the control of protein conformational dynamics by glass-forming solvents. *J Phys Chem B* 109(15):7488–7499.
12. Chung HS, Eaton WA (2013) Single-molecule fluorescence probes dynamics of barrier crossing. *Nature* 502(7473):685–8.
13. Colquhoun D, Sigworth FJ (1995) Fitting and statistical analysis of single channel records. *Single Channel Rec*:483–587.
14. Chung SH, Moore JB, Xia LG, Premkumar LS, Gage PW (1990) Characterization of single channel currents using digital signal processing techniques based on Hidden Markov Models. *Philos Trans R Soc Lond B Biol Sci* 329(1254):265–285.
15. Qin F, Auerbach A, Sachs F (2000) A direct optimization approach to hidden Markov modeling for single channel kinetics. *Biophys J* 79(4):1915–1927.
16. Hanson JA, et al. (2007) Illuminating the mechanistic roles of enzyme conformational dynamics. *Proc Natl Acad Sci* 104(46):18055–60.
17. Nir E, et al. (2006) Shot-noise limited single-molecule FRET histograms: comparison between theory

and experiments. *J Phys Chem B* 110(44):22103–24.
18. Gopich I V, Szabo A (2012) Theory of the energy transfer efficiency and fluorescence lifetime distribution in single-molecule FRET. *Proc Natl Acad Sci* 109(20):7747–52.
19. Kalinin S, Sisamakis E, Magennis SW, Felekyan S, Seidel CAM (2010) On the origin of broadening of single-molecule FRET efficiency distributions beyond shot noise limits. *J Phys Chem B* 114(18):6197–6206.
20. Chung HS, Cellmer T, Louis JM, Eaton WA (2013) Measuring ultrafast protein folding rates from photon-by-photon analysis of single molecule fluorescence trajectories. *Chem Phys* 422:229–237.
21. Berezhkovskii AM, Szabo A, Weiss GH (1999) Theory of single-molecule fluorescence spectroscopy of two-state systems. *J Chem Phys* 110(18):9145.
22. Flomenbom O, Silbey RJ (2007) Properties of the generalized master equation: Green's functions and probability density functions in the path representation. *J Chem Phys* 127(3):34103.
23. Anderson PW (1954) A Mathematical Model for the Narrowing of Spectral Lines by Exchange or Motion. *J Phys Soc Japan* 9(3):316–339.
24. Good I (1961) The Frequency Count of a Markov Chain and the Transition to Continuous Time. *Ann Math Stat* 32(1):41–48.
25. Dobrushin R (1953) Limit theorems for a markov chain of two states. *Izv Ross Akad Nauk USSR Seriya Mat* 17(4):291–330.
26. Weiss GH (1976) The two-state random walk. *J Stat Phys* 15(2):157–165.
27. Gilmore CJ (1996) Maximum Entropy and Bayesian Statistics in Crystallography: a Review of Practical Applications. *Acta Crystallogr Sect A Found Crystallogr* 52(4):561–589.
28. Ronquist F, Huelsenbeck JP (2003) MrBayes 3: Bayesian phylogenetic inference under mixed models. *Bioinformatics* 19(12):1572–1574.
29. Scheres SHW (2012) RELION: Implementation of a Bayesian approach to cryo-EM structure determination. *J Struct Biol* 180(3):519–530.
30. Bronson JE, Fei J, Hofman JM, Gonzalez RL, Wiggins CH (2009) Learning rates and states from biophysical time series: a Bayesian approach to model selection and single-molecule FRET data. *Biophys J* 97(12):3196–205.
31. van de Meent J-W, Bronson JE, Wiggins CH, Gonzalez RL (2014) Empirical Bayes Methods Enable Advanced Population-Level Analyses of Single-Molecule FRET Experiments. *Biophys J* 106(6):1327–1337.
32. Sivia DS, Skilling J (2006) *Data Analysis: A Bayesian Tutorial* (Oxford University Press, Oxford).
33. Metropolis N, Rosenbluth AW, Rosenbluth MN, Teller AH, Teller E (1953) Equation of State Calculations by Fast Computing Machines. *J Chem Phys* 21(6):1087.
34. Goodman J, Weare J (2010) Ensemble samplers with affine invariance. *Commun Appl Math Comput Sci* 5(1):65–80.
35. Foreman-Mackey D, Hogg DW, Lang D, Goodman J (2013) emcee : The MCMC Hammer. *Publ Astron Soc Pacific* 125(925):306–312.
36. Gillespie DT (1977) Exact Stochastic Simulation of Coupled Chemical Reactions. *J Phys Chem* 81(25):2340–2361.
37. Voorhees RM, Ramakrishnan V (2013) Structural basis of the translational elongation cycle. *Annu Rev Biochem* 82:203–236.
38. Fei J, Kosuri P, MacDougall DD, Gonzalez RL (2008) Coupling of ribosomal L1 stalk and tRNA dynamics during translation elongation. *Mol Cell* 30(3):348–59.
39. Fei J, et al. (2009) Allosteric collaboration between elongation factor G and the ribosomal L1 stalk directs tRNA movements during translation. *Proc Natl Acad Sci* 106(37):15702–7.
40. Frank J (2012) Intermediate states during mRNA-tRNA translocation. *Curr Opin Struct Biol* 22(6):778–85.
41. Sternberg SH, Fei J, Prywes N, McGrath KA, Gonzalez RL (2009) Translation factors direct intrinsic ribosome dynamics during translation termination and ribosome recycling. *Nat Struct Mol Biol* 16(8):861–868.
42. Fersht AR (1999) *Structure and mechanism in protein science. A guide to enzyme catalysis and protein folding* (W.H. Freeman and Co., New York).

43. Zwanzig R (2001) *Nonequilibrium Statistical Mechanics* (Oxford University Press, Oxford).
44. Van Kampen NG (2007) *Stochastic Processes in Physics and Chemistry* (North Holland, Amsterdam). 3rd Ed.
45. Hänggi P, Talkner P, Borkovec M (1990) Reaction-rate theory: fifty years after Kramers. *Rev Mod Phys* 62(2):251–341.
46. Schuler B, Lipman EA, Eaton WA (2002) Probing the free-energy surface for protein folding with single-molecule fluorescence spectroscopy. *Nature* 419(6908):743–747.
47. Soranno A, et al. (2012) Quantifying internal friction in unfolded and intrinsically disordered proteins with single-molecule spectroscopy. *Proc Natl Acad Sci* 109(44):17800–17806.
48. Chandler D (1978) Statistical mechanics of isomerization dynamics in liquids and the transition state approximation. *J Chem Phys* 68(6):2959.
49. Rabiner LR (1989) A Tutorial on Hidden Markov Models and Selected Applications in Speech Recognition. *Proc IEEE* 77(2):257–286.
50. Hill TL (2005) *Free Energy Transduction and Biochemical Cycle Kinetics* (Dover Publications, Mineola).
51. Ha T, Tinnefeld P (2012) Photophysics of fluorescent probes for single-molecule biophysics and super-resolution imaging. *Annu Rev Phys Chem* 63:595–617.
52. Cooper M, et al. (2004) Cy3B: improving the performance of cyanine dyes. *J Fluoresc* 14(2):145–50.
53. Donnert G, Eggeling C, Hell SW (2007) Major signal increase in fluorescence microscopy through dark-state relaxation. *Nat Methods* 4(1):81–86.
54. Donnert G, Eggeling C, Hell SW (2009) Triplet-relaxation microscopy with bunched pulsed excitation. *Photochem Photobiol Sci* 8(4):481–485.
55. Rasnik I, McKinney SA, Ha T (2006) Nonblinking and long-lasting single-molecule fluorescence imaging. *Nat Methods* 3(11):891–3.
56. Cordes T, Vogelsang J, Tinnefeld P (2009) On the mechanism of trolox as antiblinking and antibleaching reagent. *J Am Chem Soc* 131(14):5018–5019.
57. Altman RB, et al. (2012) Cyanine fluorophore derivatives with enhanced photostability. *Nat Methods* 9(1):68–71.
58. van der Velde JHM, et al. (2016) A simple and versatile design concept for fluorophore derivatives with intramolecular photostabilization. *Nat Commun* 7:10144.
59. Abate J, Whitt W (2006) A Unified Framework for Numerically Inverting Laplace Transforms. *INFORMS J Comput* 18(4):408–421.
60. Gibson A, Conolly B (1971) On a Three-State Sojourn Time Problem. *J Appl Probab* 8(4):716–723.
61. Berezhkovskii AM, Szabo A, Weiss GH (2000) Theory of the Fluorescence of Single Molecules Undergoing Multistate Conformational Dynamics. *J Phys Chem B* 104(16):3776–3780.
62. Gopich I V, Szabo A (2010) FRET efficiency distributions of multistate single molecules. *J Phys Chem B* 114:15221–15226.

Acknowledgements

The authors would like to thank Prof. Jan-Willem van de Meent for his comments on this manuscript. This work was supported by two NIH-NIGMS grants (R01 GM084288 and R01 GM 119386), an American Cancer Society Research Scholar Grant (RSG GMC-117152), and a Camille Dreyfus Teacher-Scholar Award (DRFSCH CU11-0665) to R.L.G. C.D.K. was supported by the Department of Energy Office of Science Graduate Fellowship Program (DOE SCGF), made possible in part by the American Recovery and Reinvestment Act of 2009, administered by ORISE-ORAU under contract number DE-AC05-06OR23100, and by Columbia University's NIH Training Program in Molecular Biophysics (T32-GM008281).

Author Contributions

C.D.K. conceived of and performed the research; C.D.K. and R.L.G. discussed results and wrote the manuscript.

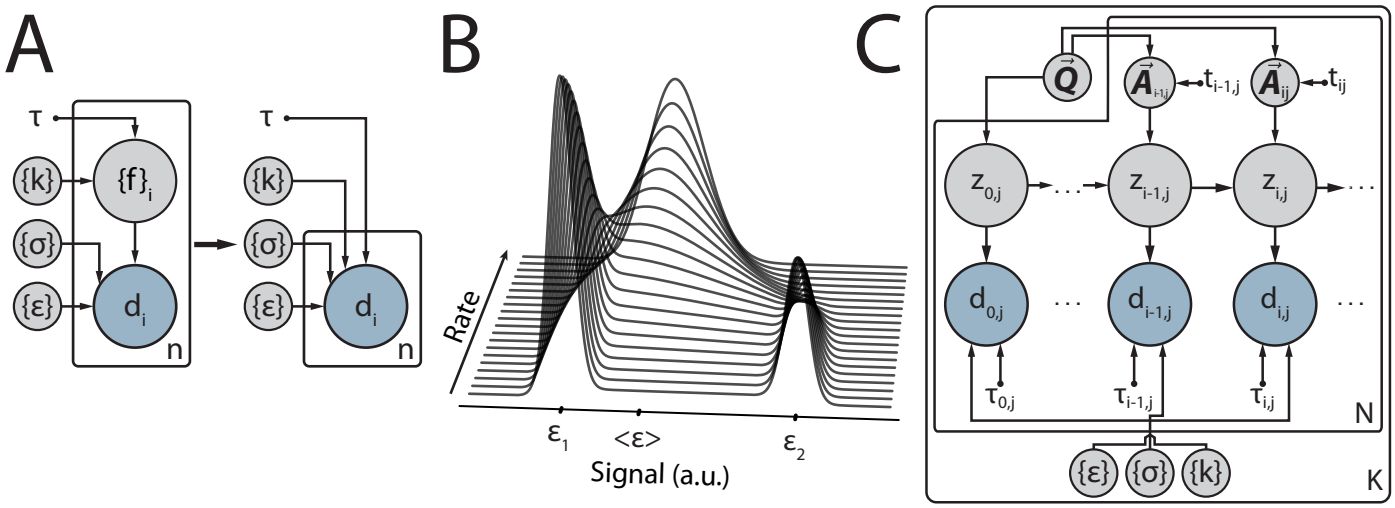

Figure 1: Graphical models for BIASD. (A) In BIASD, the dependence of the observed data point, d_i, upon the set of fractional occupancies, $\{f\}$, is marginalized to yield the graph on right, which depends upon sets of stochastic parameters $\{\varepsilon\}$, $\{\sigma\}$, and $\{k\}$, as well as upon the deterministic value of τ. (B) The marginalized, two-state likelihood function is plotted as a function of increasing rate of transitions. Arbitrary signal peaks at ε_1 and ε_2 coalesce into a single peak located at the equilibrium average $\langle\varepsilon\rangle$ as the rate constants for transitions between the two states increase relative to a fixed τ. (C) A directed graph describing hierarchical, Markovian transitions between hidden sub-temporal-resolution sub-populations is shown. The rate matrix, **Q**, dictates the steady-state probabilities, as well as transition probabilities between sub-temporal-resolution sub-populations for neighboring data points. The plates denote N signal trajectories and K sub-temporal-resolution sub-populations.

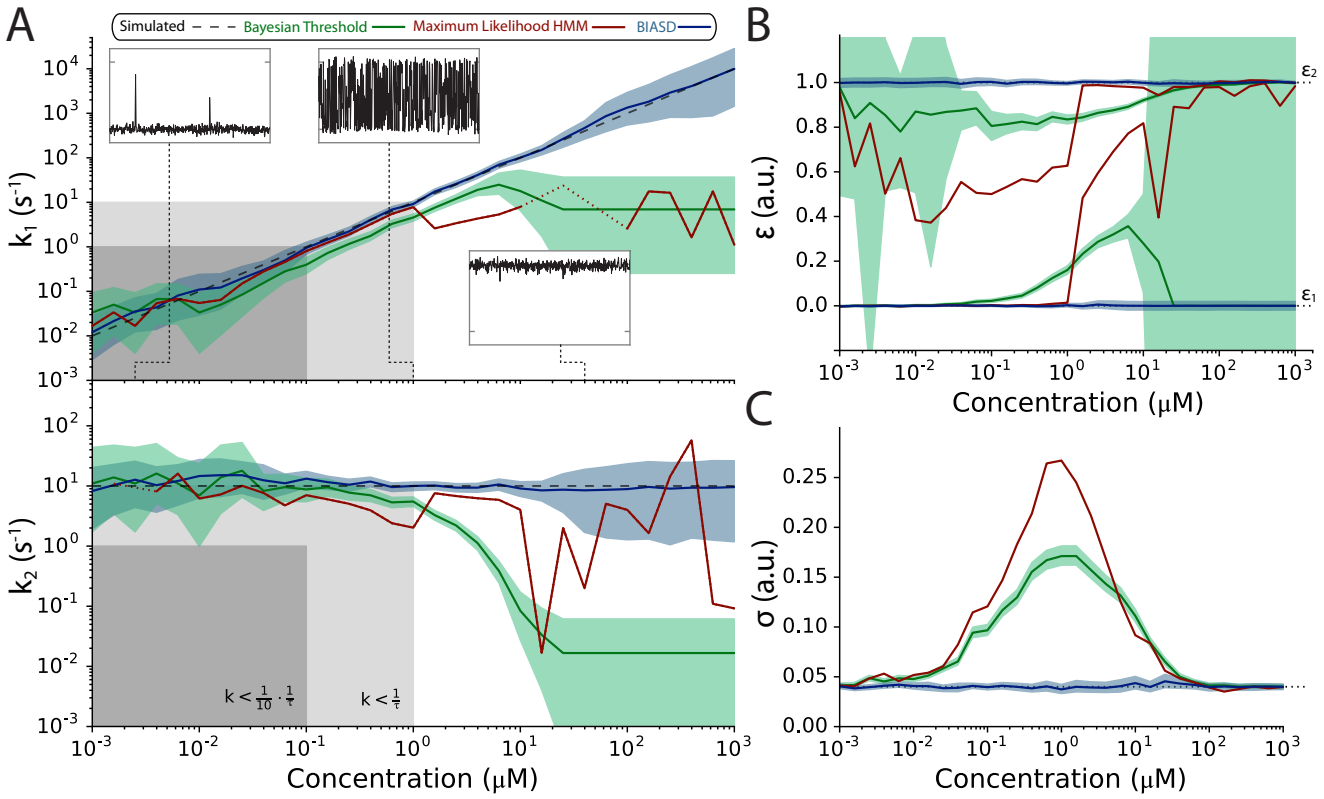

Figure 2: Analysis of k_1 and k_2 using BIASD (blue) and idealization-based (green and red) methods for a computer-simulated titration of a ligand to a receptor. [L] was varied three decades above and below the concentration where the equilibrium occupation probability of both states (K_D) is equal to 0.5. (A) Analysis of estimated rate constants k_1, and k_2. The regions where the rate constants are less than 1/10th of the acquisition rate, τ^{-1}, is shown in dark grey; the regions where the rate constants are less than the acquisition rate are shown in light grey. The simulated rate constants are plotted as the black dashed lines. The red line denotes the maximum-likelihood HMM estimate of the rate constants; dotted red lines indicate interpolated values due to transition probability estimates of unity. The green and blue areas denote the 95% credible intervals of the posterior probability distributions from analysis with half-amplitude thresholding-based Bayesian transition probability analysis (2, 13), and BIASD, respectively. Insets show the simulated signal trajectory corresponding to the indicated concentration. (B) Analysis of estimated signal values ε_1, and ε_2. Simulated values are plotted as black dashed lines. (C) Analysis of estimated signal noise σ.

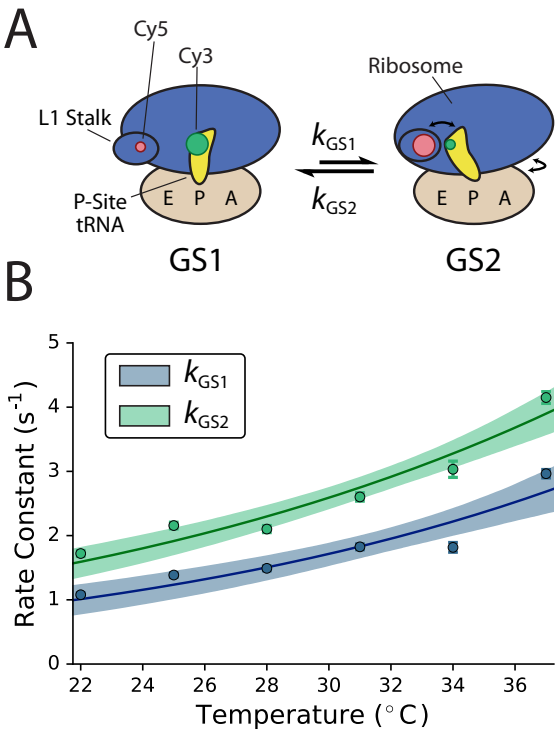

Figure 3: (A) Cartoon schematic of the GS1⇌ GS2 equilibrium on the PRE^{-A} complex previously studied by Wang and coworkers (9). Approximate positions of the Cy3 FRET donor and Cy5 FRET acceptor fluorophores of the 'L1-tRNA' labeling scheme used by Wang and coworkers are shown as green and red circles, respectively. The size of the fluorophores denotes the relative fluorescence intensity of each fluorophore in each state due to FRET. A, P, and E denote the A, P, and E sites of the ribosome, respectively. (B) Temperature dependence of k_{GS1} and k_{GS2} for PRE^{-A} complexes using BIASD. The scatter plots show the expectation value of the posterior probability distributions of k_{GS1} and k_{GS2} and the error bars represent the 95% credible interval. The solid lines denote expectation values, and the shaded regions denote the 95% credible interval of the predictive posterior probability distribution from the transition-state theory analysis.

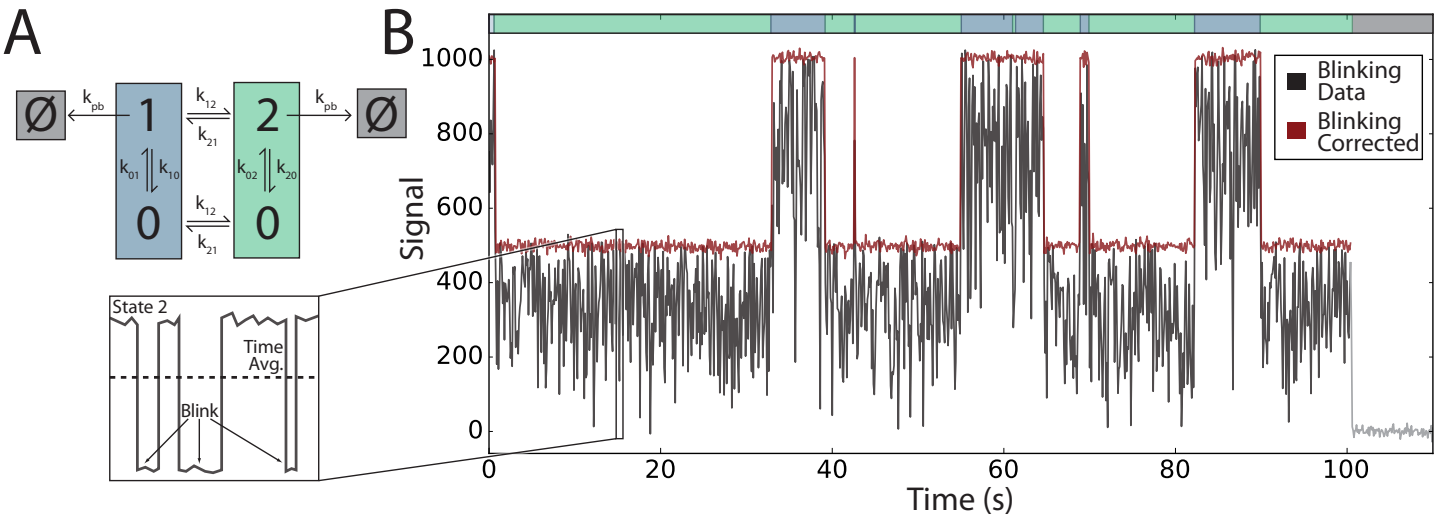

Figure 4: (A) Kinetic mechanism used to simulate an experimental system in which a biomolecule transitions between two conformational states that can each transition, with sub-temporal resolution dynamics, into and out of a photoblinked state, until eventually photobleaching. Exact values of the rate constants used in the simulation are given in the *Supporting Information*. (B) Plot of simulated signal trajectory and an estimated, corrected fluorescence intensity signal trajectory in the absence of photoblinking. The green- and blue-colored regions at the top of the plot denote the time spent in states 1 (blue) and 2 (green). The signal corrupted by sub-temporal resolution photoblinking that was analyzed by BIASD is shown in black; the inset shows a cartoon of a single τ where fast transitions are taking place between the fluorescent and photoblinked state 2. After analysis with BIASD, the MAP solution of the posterior probability distribution was used to generate a Viterbi-idealized path, which is plotted in red with noise added back from the MAP value of σ; this is a plausible corrected fluorescence intensity signal trajectory in the absence of photoblinking. While one excursion to state 2 is not present in this Viterbi path, the forward-backward algorithm used in the HMM analysis takes it into consideration.